

# Dynamic light scattering Monte Carlo: a method for simulating time-varying dynamics for ordered motion in heterogeneous media

Mitchell A. Davis<sup>1</sup> and Andrew K. Dunn<sup>2\*</sup>

<sup>1</sup> Department of Electrical and Computer Engineering, The University of Texas at Austin, Austin, Texas 78712, USA

<sup>2</sup> Department of Biomedical Engineering, The University of Texas at Austin, Austin, TX 78712, USA

[\\*adunn@utexas.edu](mailto:adunn@utexas.edu)

**Abstract:** Few methods exist that can accurately handle dynamic light scattering in the regime between single and highly multiple scattering. We demonstrate dynamic light scattering Monte Carlo (DLS-MC), a numerical method by which the electric field autocorrelation function may be calculated for arbitrary geometries if the optical properties and particle motion are known or assumed. DLS-MC requires no assumptions regarding the number of scattering events, the final form of the autocorrelation function, or the degree of correlation between scattering events. Furthermore, the method is capable of rapidly determining the effect of particle motion changes on the autocorrelation function in heterogeneous samples. We experimentally validated the method and demonstrated that the simulations match both the expected form and the experimental results. We also demonstrate the perturbation capabilities of the method by calculating the autocorrelation function of flow in a representation of mouse microvasculature and determining the sensitivity to flow changes as a function of depth.

© 2015 Optical Society of America

**OCIS codes:** (290.4210) Multiple scattering; (290.7050) Turbid media; (170.6480) Spectroscopy, speckle; (170.3340) Laser Doppler velocimetry

---

## References and links

1. B. J. Berne and R. Pecora, *Dynamic Light Scattering: With Applications to Chemistry, Biology, and Physics* (Dover, 2000).
2. N. Ben-Yosef, "Mass motion as observed by light-beating spectroscopy," *Appl. Phys. Lett.* **21**, 436 (1972).
3. T. Tanaka and G. B. Benedek, "Measurement of the Velocity of Blood Flow (in vivo) Using a Fiber Optic Catheter and Optical Mixing Spectroscopy," *Appl. Opt.* **14**, 189–196 (1975).
4. B. Berne and R. Pecora, "Laser light scattering from liquids," *Annu. Rev. Phys. Chem.* **25**, 233–253 (1974).
5. D. Pine, D. Weitz, J. Zhu, and E. Herbolzheimer, "Diffusing-wave spectroscopy: dynamic light scattering in the multiple scattering limit," *J. Phys.* **51**, 2101–2127 (1990).
6. D. A. Boas and A. G. Yodh, "Spatially varying dynamical properties of turbid media probed with diffusing temporal light correlation," *JOSA A* **14**, 192–215 (1997).
7. D. Bicoût and G. Maret, "Multiple light scattering in Taylor-Couette flow," *Phys. A Stat. Mech. its Appl.* **210**, 87–112 (1994).
8. X.-L. Wu, D. J. Pine, P. M. Chaikin, J. S. Huang, and D. A. Weitz, "Diffusing-wave spectroscopy in a shear flow," *J. Opt. Soc. Am. B* **7**, 15 (1990).
9. P. Zakharov, A. C. Völker, M. T. Wyss, F. Haiss, N. Calcinaghi, C. Zunzunegui, A. Buck, F. Scheffold, and B. Weber, "Dynamic laser speckle imaging of cerebral blood flow," *Opt. Express* **17**, 13904–13917 (2009).

10. D. D. Duncan and S. J. Kirkpatrick, "Can laser speckle flowmetry be made a quantitative tool?" *J. Opt. Soc. Am. A. Opt. Image Sci. Vis.* **25**, 2088–2094 (2008).
11. A. Fercher and J. Briers, "Flow visualization by means of single-exposure speckle photography," *Opt. Commun.* **37**, 326–330 (1981).
12. D. A. Boas and A. K. Dunn, "Laser speckle contrast imaging in biomedical optics," *J. Biomed. Opt.* **15**, 011109–1–12 (2010).
13. C. Urban and P. Schurtenberger, "Characterization of Turbid Colloidal Suspensions Using Light Scattering Techniques Combined with Cross-Correlation Methods," *J. Colloid Interface Sci.* **207**, 150–158 (1998).
14. P. Zakharov, A. Völker, A. Buck, B. Weber, and F. Scheffold, "Quantitative modeling of laser speckle imaging," *Opt. Lett.* **31**, 3465–3467 (2006).
15. W. V. Meyer, D. S. Cannell, a. E. Smart, T. W. Taylor, and P. Tin, "Multiple-scattering suppression by cross correlation," *Appl. Opt.* **36**, 7551–7558 (1997).
16. F. F. de Mul, M. H. Koelink, M. L. Kok, P. J. Harmsma, J. Greve, R. Graaff, and J. G. Aarnoudse, "Laser Doppler velocimetry and Monte Carlo simulations on models for blood perfusion in tissue," *Appl. Opt.* **34**, 6595–6611 (1995).
17. V. Asadpour, M. Miranbeigi, F. Towhidkhal, and M. Khosroshahi, "Laser-Doppler blood-flowmetry modeling by Monte Carlo method," 2001 Conf. Proc. 23rd Annu. Int. Conf. IEEE Eng. Med. Biol. Soc. **4**, 3252–3254 (2001).
18. R. Bonner and R. Nossal, "Model of laser Doppler measurements of blood flow in tissue," *Appl. Opt.* **20**, 2097–2107 (1981).
19. T. Pfeifer, J. Kehlet Barton, E. Chan, M. Ducros, B. Sorg, T. Milner, J. Nelson, and A. Welch, "A three-dimensional modular adaptable grid numerical model for light propagation during laser irradiation of skin tissue," *IEEE J. Sel. Top. Quantum Electron.* **2**, 934–942 (1996).
20. D. A. Boas, J. Culver, J. Stott, and A. Dunn, "Three dimensional Monte Carlo code for photon migration through complex heterogeneous media including the adult human head," *Opt. Express* **10**, 159–170 (2002).
21. M. A. Davis, S. M. Shams Kazmi, A. Ponticorvo, and A. K. Dunn, "Depth dependence of vascular fluorescence imaging," *Biomed. Opt. Express* **2**, 3349–3362 (2011).
22. M. A. Davis, S. M. S. Kazmi, and A. K. Dunn, "Imaging depth and multiple scattering in laser speckle contrast imaging," *J. Biomed. Opt.* **19**, 86001 (2014).
23. W. Groop, E. L. Lusk, and A. Skjellum, *Using MPI: Portable Parallel Programming with the Message Passing Interface* (MIT Press, 1999).
24. M. Mascagni and A. Srinivasan, "Algorithm 806: SPRNG: A scalable library for pseudorandom number generation," *ACM Trans. Math. Softw.* **26**, 436–461 (2000).
25. Q. Fang, "Mesh-based Monte Carlo method using fast ray-tracing in Plücker coordinates," *Biomed. Opt. Express* **1**, 165–175 (2010).
26. E. Alerstam, T. Svensson, and S. Andersson-Engels, "Parallel computing with graphics processing units for high-speed Monte Carlo simulation of photon migration," *J. Biomed. Opt.* **13**, 060504 (2008).
27. C. K. Hayakawa, J. Spanier, F. Bevilacqua, A. K. Dunn, J. S. You, B. J. Tromberg, and V. Venugopalan, "Perturbation Monte Carlo methods to solve inverse photon migration problems in heterogeneous tissues," *Opt. Lett.* **26**, 1335–1337 (2001).
28. S. Preibisch, S. Saalfeld, and P. Tomancak, "Globally optimal stitching of tiled 3D microscopic image acquisitions," *Bioinformatics* **25**, 1463–1465 (2009).
29. A. F. H. McCaslin, B. R. Chen, A. J. Radosevich, B. Cauli, and E. M. C. Hillman, "In vivo 3D morphology of astrocyte-vasculature interactions in the somatosensory cortex: implications for neurovascular coupling," *J. Cereb. blood flow Metab.* **31**, 795–806 (2011).
30. P. S. Tsai, J. P. Kaufhold, P. Blinder, B. Friedman, P. J. Drew, H. J. Karten, P. D. Lyden, and D. Kleinfeld, "Correlations of neuronal and microvascular densities in murine cortex revealed by direct counting and colocalization of nuclei and vessels," *J. Neurosci.* **29**, 14553–14570 (2009).
31. M. Meinke, G. Müller, J. Helfmann, and M. Friebe, "Empirical model functions to calculate hematocrit-dependent optical properties of human blood," *Appl. Opt.* **46**, 1742–1753 (2007).
32. A. N. Yaroslavsky, P. C. Schulze, I. V. Yaroslavsky, R. Schober, F. Ulrich, and H. J. Schwarzmaier, "Optical properties of selected native and coagulated human brain tissues in vitro in the visible and near infrared spectral range," *Phys. Med. Biol.* **47**, 2059–2073 (2002).

---

## 1. Introduction

Dynamic light scattering techniques have been used since the 1960s to characterize the motion of particles [1]. In the single scattering regime, several methods have been developed to measure either flowing or diffusing particles [2–4]. Likewise, the theory behind particle motion characterization in highly multiple scattering media, often called Diffusing Wave Spectroscopy

(DWS), is also well developed [5–8]. However, in the intermediate scattering regime, where a significant amount of light travels less than two or three reduced mean free paths, theoretical modeling becomes very difficult and sample dependent [9]. These models also require an assumption about the form of the autocorrelation function, where the usual assumption is either Gaussian or Lorentzian [10]. Furthermore, in wide field imaging methods such as Laser Speckle Contrast Imaging (LSCI), the detected signal is a mixture of photons from all scattering regimes [11, 12]. Several experimental methods have been developed that are designed to suppress multiple scattering [13–15]. While effective, these methods increase the complexity of otherwise simple instrumentation.

Here we demonstrate dynamic light scattering Monte Carlo (DLS-MC), a numerical technique which leverages the increases in computational power to directly model dynamic light scattering in an arbitrary three dimensional voxelized geometry. The advantage to this approach is that it does not require assumptions about the degree of multiple scattering or the form of the autocorrelation function. The method is similar to Monte Carlo based models designed to simulate laser Doppler flowmetry, but results in the field autocorrelation function rather than the Doppler power spectra [16, 17]. Furthermore, this method is capable of rapidly evaluating the effect of particle motion changes in the geometry.

## 2. Theory

### 2.1. Dynamic light scattering

The electric field autocorrelation function  $g_1(t)$  is defined as

$$g_1(t) = \langle E(0)E^*(t) \rangle \quad (1)$$

which describes the effects of particle motion on the electric field. As mentioned before, the laser Doppler and DWS literature is full of examples where the form of  $g_1(\tau)$  is calculated by making assumptions regarding the nature of the particles in motion [1, 3, 18]. These methods begin by assuming the form of the incident E-field to be a plane wave:

$$E_i = E_0(\mathbf{r}) \exp(j\mathbf{k} \cdot \mathbf{r}) \quad (2)$$

where  $E_0(\mathbf{r})$  is the amplitude of the incident field at the point  $\mathbf{r}$  and  $\mathbf{k}$  is the wavevector.

When the incident field scatters from a moving particle at location  $\mathbf{r}$  in the medium, the resulting scattered electric field has the following form [6]:

$$E_s(R, t) = A(\mathbf{r})E_0(\mathbf{r}) \exp(j\mathbf{k}_f \cdot \mathbf{R}) \exp(-j(\mathbf{k}_f - \mathbf{k}_i) \cdot \mathbf{r}(t)) \quad (3)$$

where  $A(\mathbf{r})$  is the amplitude loss from absorption during the scattering event,  $\mathbf{k}_f$  is the scattered field wavevector,  $\mathbf{k}_i$  is the incident field wavevector,  $\mathbf{R}$  is the scattering volume, and  $r(t)$  is the location of the scattering particle within that scattering volume. For convenience, the scattering vector  $\mathbf{q}$  is defined as:

$$\mathbf{q} = \mathbf{k}_f - \mathbf{k}_i, \quad (4)$$

which has a magnitude of  $q = 2k_0 \sin(\theta/2)$ , where  $k_0$  is the wavenumber and  $\theta$  is the angle between the incident and scattered field wavevectors. From here, one can use the definition of the field autocorrelation function  $g_1(t)$  along with the definition of the scattered field to arrive at:

$$g_1(t) = \langle E(0)E^*(t) \rangle = \langle A(\mathbf{r})|E_0(\mathbf{r})|^2 \exp(j\mathbf{q} \cdot [\mathbf{r}(t) - \mathbf{r}(0)]) \rangle \quad (5)$$

where  $[\mathbf{r}(t) - \mathbf{r}(0)]$  describes the motion of the scattering particle [1].

Previous work has included the effects of multiple scattering by accumulating the phase shift attributed to each scattering event along the photon path [6, 16]. Using the relationship

$\mathbf{q} = 2k_0 \sin(\theta/2)\hat{\mathbf{q}}$ , where  $\hat{\mathbf{q}}$  is the unit vector of  $\mathbf{q}$ , the effective contribution to  $g_1(t)$  from a single photon path with  $N$  dynamic scattering events is:

$$E(0)E^*(t) = A(\mathbf{r})|E_0(\mathbf{r})|^2 \exp(j2k_0t \sum_n^N (\sin(\frac{\theta_n}{2})\hat{\mathbf{q}}_n \cdot \mathbf{V}_n)). \quad (6)$$

where  $\mathbf{V}_n$  is the velocity of the particle at scattering event  $n$ . The unique aspects of any given photon path length incident on the detector are the absorption weighting  $A$  and the cumulative phase shifts in the sum corresponding to each dynamic scattering event along the photon path. For convenience, the scalar value  $Y$  is defined as  $\sum_n (\sin(\frac{\theta_n}{2})\hat{\mathbf{q}}_n \cdot \mathbf{V}_n)$ . The expectation of the absorption weighted sum of Eq. (6) over all photon paths gives  $g_1(t)$ :

$$g_1(t) = \langle E(0)E^*(t) \rangle = \int_{-\infty}^{\infty} P(Y) \exp(j2k_0Yt) dY. \quad (7)$$

This expression makes no assumption about the number of dynamic scattering events or the degree of correlation between successive scattering events. The values  $Y$  and  $P(Y)$  can be calculated using the Monte Carlo model of light transport if the vector directions of particle movement are known or assumed.

## 2.2. Dynamic Monte Carlo simulations

Monte Carlo simulations are often used for evaluating the transport of light through turbid media. To solve Eq. (7), a three dimensional voxelized Monte Carlo model was used. Unlike layered models used in early simulations of Doppler scattering, three dimensional models offer the advantage of being applicable to a wider range of potential problems [19–22]. An example of this increased flexibility is demonstrated later where the autocorrelation function is calculated for an imaging setup using a three dimensional representation of brain microvasculature.

The two primary inputs required to solve Eq. (7) are the photon path through the medium and the vector direction of flow at each scattering event. Each voxel of the Monte Carlo geometry is given optical properties that determine the distribution of photon scattering lengths, degree of absorption, and the scattering angle phase function. The Henyey-Greenstein phase function was used with corresponding anisotropy  $g$ . The illumination consists of a diverging cone of light incident on the surface of the geometry. Detection occurs when a photon scatters through the medium and is incident on a specified detection surface.

To evaluate light transport in complex media, many photons must be simulated to allow the distribution of photon paths to converge. In some cases, depending on the size of the geometry, illumination radius, and size of the region of interest (ROI), as many as  $10^9 - 10^{10}$  photons must be simulated. However, since each launched photon is statistically independent, many simulations can be initialized simultaneously as long as the random number generators produce statistically independent values. Parallelization of the code was performed using the message passing interface (MPI) [23]. Using MPI, Monte Carlo simulations could be simultaneously initialized on an arbitrary number of processor cores. The Scalable Parallel Pseudo Random Number Generator (SPRNG) was used to ensure statistical independence among the parallel simulation instances [24]. Here the model is parallelized using the MPI library and is run on the Lonestar cluster at the Texas Advanced Computing Center (TACC). With this setup, up to 4000 independent simulation threads may be launched simultaneously, which easily provides enough computing power to allow convergence.

While this work used the above Monte Carlo method to calculate photon propagation through heterogeneous media, the DLS-MC method does not require this specific implementation. Any implementation may be used, such as a GPU accelerated Monte Carlo or a meshed based Monte Carlo, as long as it is modified to save the photon scattering coordinates to a database [25, 26].

For each detected photon, the coordinates of each scattering location and the absorption-adjusted weight of the photon is saved for post-processing. These values, along with the vector direction of flow at each point, are sufficient to solve for  $g_1(t)$  as shown in Eq. (7).

Typically, the Monte Carlo simulations are performed such that all photons exiting the detection surface are recorded. It is often appropriate to then specify a smaller region of interest on the surface, and use only photons which exited the surface in that region with a given NA. For each detected photon  $i$ , the dynamic contribution  $Y_{i,n}$  of each scattering event along the photon's path may be calculated using the following expression:

$$Y_{i,n} = (\hat{k}_{f,n} - \hat{k}_{i,n}) \cdot \mathbf{V}_n \quad (8)$$

where  $\hat{k}_{f,n}$  is the unit wavevector after scattering,  $\hat{k}_{i,n}$  is the unit vector before scattering, and  $\mathbf{V}_n$  is the vector direction of flow in the medium at the coordinates where scattering event  $n$  occurs.

The contribution of each photon path to  $g_1(\tau)$  is determined by the absorption weighted value of the detected photons along its path [27]. The absorption weighted value  $w_i$  for each photon path is:

$$w_i = \prod_j \exp(-\mu_a^j l_{ij}) \quad (9)$$

where  $\mu_a^j$  is the absorption coefficient of material  $j$  and  $l_{ij}$  is the path length of photon  $i$  through material  $j$ .  $M$  is the total number of detected photons used in the calculation of  $g_1(t)$ . The value of  $P(Y_i)$  is determined by dividing the absorption weighted value by the sum of all detected photon's weights:

$$P(Y_i) = \frac{w_i}{\sum_i^M w_i} \quad (10)$$

Once the photon weight  $P(Y_i)$  and the dynamic contribution from each scattering event  $Y_{in}$  have been calculated for each photon, they are stored to a database along with the number of dynamic scattering events  $N_i$  and the coordinates of each scattering event for further processing.

### 2.3. Calculation of the autocorrelation function

Using the recorded photon weight and dynamic scattering event contributions, the autocorrelation function is calculated by taking the expected value over all simulated photon paths:

$$g_1(t) = \sum_{i=1}^M P(Y_i) \exp(jk_0 t \sum_{n=1}^N Y_{i,n}). \quad (11)$$

where  $M$  is the number of detected photons and  $N$  is the number of dynamic scattering events of photon  $i$ . Note that the factor of 2 and the  $\sin(\theta/2)$  terms are missing in comparison to Eq. (7) because  $Y$  is defined differently. Both expressions are equally valid.

One of the advantages of the presented method is that  $g_1(t)$  may be re-calculated using different flow conditions while the photon paths remain the same. Since each value  $Y_{i,n}$  is proportional to the velocity at the scattering coordinates of event  $n$  of photon  $i$  (which are also recorded), they may be re-scaled to reflect a new velocity and the autocorrelation function can be re-calculated.

Perturbations are defined by specifying a volume and the magnitude of velocity change. Using the coordinate bounds of the perturbed volume, the individual dynamic scattering events from all photons that occur inside the volume are scaled by the magnitude of the perturbation. The sum of all dynamic scattering events  $Y_{i,n}$  from each photon is re-calculated, and the ensemble average of all photons is re-calculated according to Eq. (11).

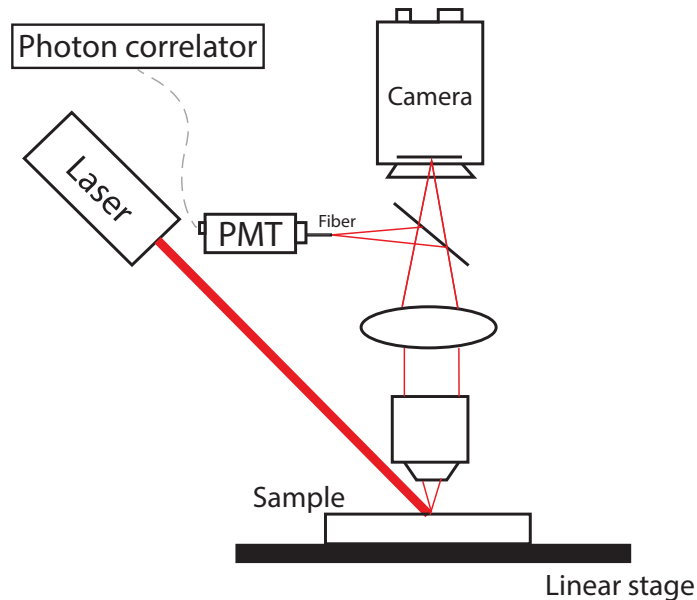


Fig. 1. Autocorrelation measurement setup for PDMS phantom experiments.

Using this perturbation method allows for the determination of differential autocorrelation time changes that depend only on the change in the flow conditions. The noise associated with the photon path information is shared among all calculations. Because all the required information can be stored in memory or a database, the re-calculation of  $g_1(t)$  can be performed quickly. This removes the need to perform many separate, independent simulations when using the same geometry. As with other perturbation Monte Carlo methods [27], this could potentially be used to solve inverse problems in dynamic media.

### 3. Experimental validation

To evaluate the ability of the model to accurately predict both the form and the effect of perturbations on  $g_1(t)$ , an experimental validation was performed using phantoms under linear motion. We measured the intensity autocorrelation function,  $g_2(t)$ , and calculated the field autocorrelation function through the Siegert relation:

$$g_2(t) = B(1 + \beta |g_1(t)|^2) \quad (12)$$

where  $\beta$  is an experimental instrumentation factor and  $B$  is an offset.

Experimental measurements of  $g_2(t)$  were performed using a poly-dimethyl-siloxane (PDMS) phantom. The PDMS was mixed with 1.8 mg/g titanium dioxide ( $TiO_2$ ). As shown in Fig. 1, an actuated microscope stage was used to move the phantom at a fixed rate of 0.1 - 1.0 mm/s. The surface of the phantom was illuminated using a 660nm laser diode. The scattered light was collected by a single mode fiber connected to a photomultiplier tube (Hamamatsu) and measured using a photon correlator board (DPC 130, Becker and Hickl). The

intensity autocorrelation function was calculated from the experimental data for a time range of  $10^{-7} - 10^{-1}$  s. Approximately  $10^7 - 10^8$  photons were collected over the course of 30 seconds during each experiment to ensure that noise at the longer times was low enough to not obscure the form of the autocorrelation function.

DLS-MC simulations were performed using a voxelized geometry representation of the phantom. The optical properties of the PDMS phantom at 660nm were:  $\mu_s = 8 \text{ mm}^{-1}$ ,  $\mu_a = 0.001 \text{ mm}^{-1}$ , and  $g = 0.9$ . The Zemax optical ray tracing software package was used to determine the correct detector NA for use in the simulations, which was approximately 0.03. The corresponding velocities were uniform and matched to the experimental stage values (0.1 - 1.0 mm/s). Since the perturbation method described above was used to change the velocity and re-calculate the autocorrelation function, only one Monte Carlo simulation was required.

#### 4. Cortical blood flow simulations

To demonstrate the flexibility and perturbation capabilities of DLS-MC in heterogeneous media, the autocorrelation function corresponding to cortical blood flow in a mouse was calculated. The velocities in each layer of the geometry were then perturbed and the change in the autocorrelation time constant  $\tau_c$  of  $g_1(t)$  was determined. The autocorrelation time constant  $\tau_c$  is defined as in an exponential distribution: the time at which the normalized  $g_1(t)$  curve reaches a value of  $\frac{1}{e}$ .

The vascular geometry was obtained from two photon fluorescence stacks of mouse cortical vasculature. Four overlapping  $600 \mu\text{m} \times 600 \mu\text{m}$  image stacks were taken in  $2 \mu\text{m}$  axial steps down to  $500 \mu\text{m}$ . The image stacks were stitched together using the method developed by Preibisch et. al. to create one large  $1024 \mu\text{m} \times 1024 \mu\text{m} \times 500 \mu\text{m}$  image stack [22, 28]. The stack was then extended down to  $900 \mu\text{m}$  in depth by matching vascular volume fractions to 3-6% as reported in McCaslin et al. by replicating the capillary bed layers already present between 250-450  $\mu\text{m}$  in the image stack [29]. The stacks were then vectorized using the semi-automated VIDA Suite followed by manual correction to determine the direction of the vessel centerlines [30]. The sign of the flow vector (+/- relative to segmented centerline direction) for each vessel strand was chosen randomly, and a fixed speed of 1 mm/s was used for capillaries and 5 mm/s for non-capillaries. Optical properties were assigned separately to vessels with a diameter smaller than 11  $\mu\text{m}$  (capillaries) and larger than 11  $\mu\text{m}$  based on an assumed capillary hematocrit (Hct) of 15 % and a non-capillary Hct of 45 %.

Table 1. Optical properties for microvasculature geometry

	$\mu_a$ ( $\text{mm}^{-1}$ )	$\mu_s$ ( $\text{mm}^{-1}$ )	$g$
Capillaries	0.20	60	0.98
Non-capillaries	0.20	95	0.98
Extravascular	0.02	10	0.90

The intravascular absorption and scattering coefficients were interpolated from measurements done by Meinke et al [31]. Extravascular absorption and scattering coefficients were based on the *in vitro* measurements by Yaroslavsky et al [32]. It was necessary to use *in vitro* measurements of the extravascular tissue because blood was assumed to only be present in intravascular space. The *in vitro* measurements were taken in the absence of blood. Table 1 lists the optical properties used in these simulations.

Camera-based detection optics were used for these simulations, which models the commonly used LSCI imaging method [12]. A 1 mm collimated beam was used to illuminate the surface of the geometry, and a 30  $\mu\text{m}$  square region of interest (ROI) with an NA of 0.25 was used as

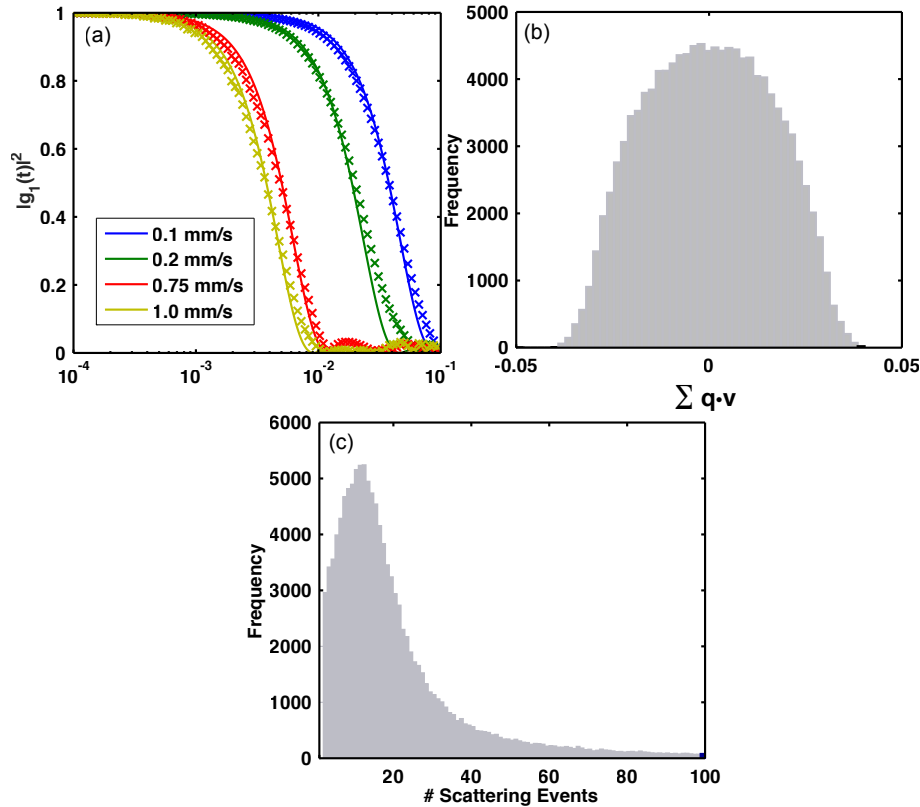


Fig. 2. Comparison of experimental and simulation results from PDMS phantom experiment. (a) Shows the simulation (-) and experimental (x) results at four different constant linear speeds. (b) and (c) show the simulated histograms of  $\mathbf{q} \cdot \mathbf{v}$  and the number of scattering events.

the detector to mimic a single camera pixel. Two ROIs were chosen, one over a large surface vessel and one over a region without surface vessels.

The depth-dependent flow contribution to the autocorrelation function was determined by successively reducing the flow of each  $50 \mu\text{m}$  layer of the geometry to 5% of the baseline flow. To perform the perturbation, the values  $Y_{i,n}$  which arise from coordinates inside the perturbed region are scaled by 0.05 and the autocorrelation function is recalculated according to Eq. (11). The autocorrelation time constant  $\tau_c$  was determined and the baseline  $\tau_c$  from the unperturbed calculation was subtracted to determine the change in  $\tau_c$  corresponding to flow in each layer.

## 5. Results

### 5.1. Experimental validation

Using the DLS-MC method,  $1 \times 10^9$  photons were simulated in approximately 5 minutes using 200 cores on the TACC Lonestar cluster. A  $150 \mu\text{m} \times 150 \mu\text{m}$  ROI resulted in approximately  $8 \times 10^7$  detected photons in the Monte Carlo simulation. Calculation of  $g_1$  using the photon scattering coordinates and the velocity data took less than 2 minutes.

Figure 2 shows the results of the comparison between the PDMS phantom measurements and simulations. In Fig. 2(a) shows the squared electric field autocorrelation function for both the



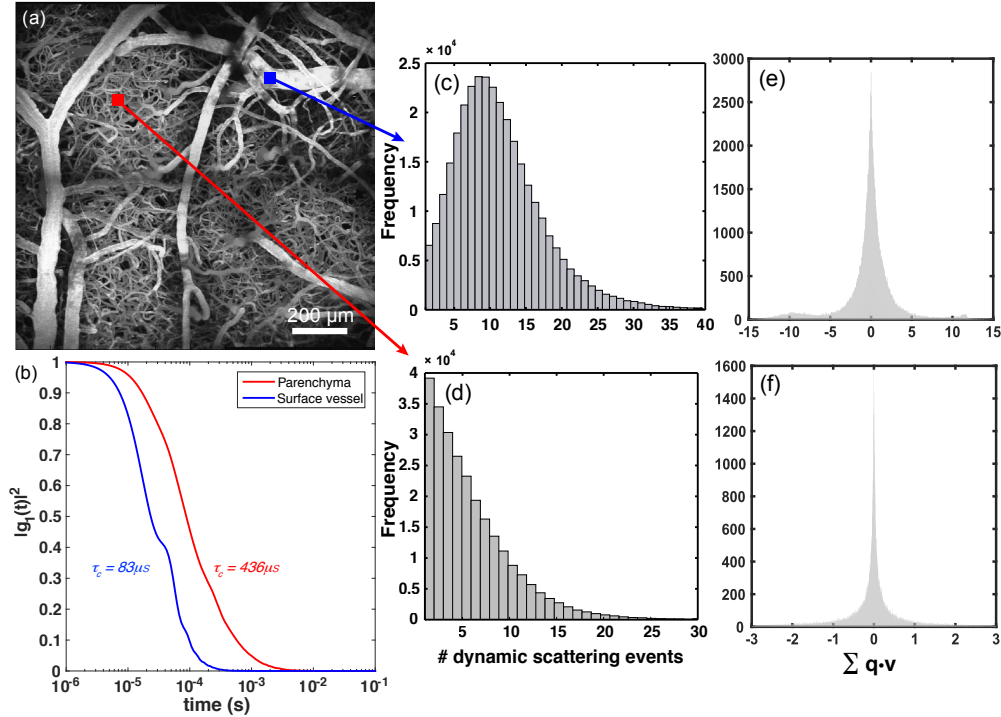


Fig. 3. Example calculation of autocorrelation function of mouse cortical microvasculature. Two photon maximum intensity projection of microvasculature stack is shown in (a).

experimental measurements and the simulations. Figure 2(b) shows the distribution of the inner product of the scattering and velocity vectors in the simulation when  $v = 1.0$  mm/s. In the case of constant uniform motion, the successive scattering vectors cancel out and  $\sum_{i=1}^N q_i = k_N - k_1$ . Given that the velocity vector is nearly perpendicular to both the entering and exiting wavevectors, the  $\mathbf{q} \cdot \mathbf{v}$  value is primarily a function of the NA of the illumination (0.01) and detection (0.03). Figure 2(c) shows the histogram of the number of scattering events experienced by photons in the simulations. This provides additional verification that the numerical method is performing as expected, as the  $\mathbf{q} \cdot \mathbf{v}$  value is unchanged and depends only on  $k_N$  and  $k_i$ , even though the photons undergo a significant number of dynamic scattering events, all of which are included in the calculation of the simulated  $g_1(t)$ .

### 5.2. Cortical blood flow simulations

The results of the microvasculature simulation are shown in Fig. 3. The ROIs of the surface vessel and non surface vessel ROIs are shown as overlays in Fig. 3(a). The form of  $|g_1(\tau)|^2$  shown in Fig. 3(b) shows a significant difference between the two ROIs. This is unsurprising as the speed in the targeted surface vessel is 5.0 mm/s, whereas the speed in capillaries is 1.0 mm/s. Furthermore, the surface vessel autocorrelation function decays significantly faster for two other reasons.

First, the surface vessel ROI has significantly more dynamic scattering events on average, as shown in Figs. 3(c)–3(d). Each dynamic scattering event along a photons path generates an additional phase accumulation term, so even with a uniform velocity the ROI with more scattering events will decay more quickly.

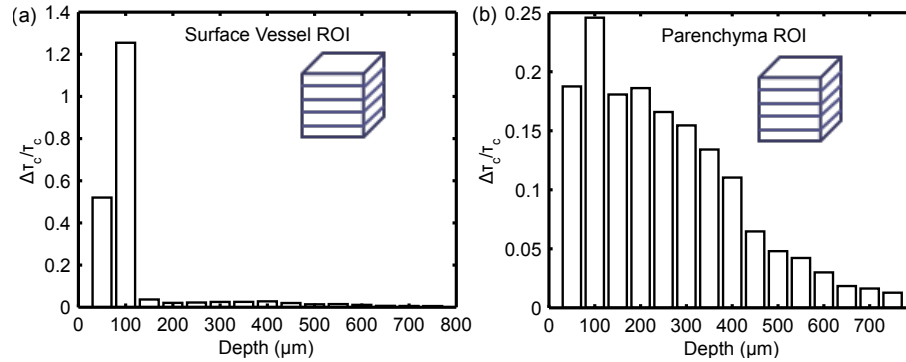


Fig. 4. The change in  $\tau_c$  from a 95% change in flow velocity for the (a) surface vessel ROI and (b) parenchyma ROI in each  $50\ \mu\text{m}$  layer of the geometry.

Additionally, the photons traveling through the surface vessel undergo multiple highly correlated sequential scattering events. This manifests as the asymmetrical features in the distribution of  $\mathbf{q} \cdot \mathbf{v}$  in Fig. 3(e). Since the photons traveling primarily through the capillary bed usually scatter only once per vessel, the distribution of  $\mathbf{q} \cdot \mathbf{v}$  shown in Fig. 3(f) is more symmetrical.

The sensitivity of  $\tau_c$  to changes in flow velocity are shown in Fig. 4 for the surface vessel and parenchyma ROI shown in Fig. 3(a). For each  $50\ \mu\text{m}$  perturbed layer, the autocorrelation function took approximately 10 seconds to calculate. The depth-dependent sensitivity required 30 perturbation volumes to represent the top  $750\ \mu\text{m}$  as shown in Fig. 4. While the changes in  $\tau_c$  shown are calculated using assumed velocity values, they do demonstrate the utility of the DLS-MC method to determine the sensitivity of  $g_1(t)$  to flow changes.

The depth-dependent changes in  $\tau_c$  show that the surface vessel ROI sensitivity in Fig. 4(a) is strongly weighted towards the surface of the geometry. By contrast, the parenchyma ROI in Fig. 4(b) demonstrates a slower decline of sensitivity with increasing depth into the tissue.

## 6. Discussion

The results demonstrate that this method is capable of generating distributions of the scattering phase (i.e.  $\mathbf{q} \cdot \mathbf{v}$ ) that were previously not predicted by analytical methods. For example, in the case of the surface vessel ROI shown in Fig. 3(e), the distribution of  $\mathbf{q} \cdot \mathbf{v}$  contains additional features which could not be predicted by traditional analytical formulations.

The commonly used distributions are assumptions based on the predicted (or simplified) nature of dynamic interactions between photons and moving particles. The Gaussian distribution is a good assumption when successive dynamic scattering events are independent, or when photons scatter only once dynamically and each particle trajectory is independent. This requirement is met in some conditions. For example, when particles are diffusing in a random-walk, the particle direction at any time  $t$  is independent of every other time. Dynamic interactions between photons and diffusing particles are, therefore, independent and follow a Gaussian distribution.

However, when the system has regions of ordered flow, as in the example of perfused brain tissue, the photon-particle interactions are not always independent. In the capillary bed, where the complex network of vessels are arranged somewhat randomly and photons scatter only once in each vessel, the successive dynamic scattering events can be said to be independent. In larger vessels (arterioles, arteries, veins, etc), where photons scatter more than once before exiting the vessel, the independence assumption breaks down. In this case, the commonly used distributions are not sufficient to separate the effects of increased particle velocity and increased fluid volume.

Furthermore, the depth-dependent change in  $\tau_c$  shown in Fig. 4 demonstrates the possibility of using the DLS-MC method to determine the sensitivity of dynamic light scattering techniques to changes in flow velocity. Perturbation based Monte Carlo methods have the advantage of sharing noise among each separate calculation [27], which allows for a more precise determination of the effect of particle velocity changes on the time varying dynamics of the system.

## 7. Conclusion

We have demonstrated a numerical method by which the electric field autocorrelation function is calculated for arbitrary geometries. The method makes no assumptions regarding the number of scattering events, the final form of the autocorrelation function, or the degree of correlation between scattering events. We have validated the method using static PDMS phantoms and verified that the simulations match both the expected form and the experimental results. Finally, we demonstrated the utility and perturbation-capabilities of the method by calculating the autocorrelation function of flow in a representation of mouse microvasculature and calculating the sensitivity to flow changes as a function of depth.

## Acknowledgments

We gratefully acknowledge support from the Consortium Research Fellows Program, ORISE Research Participation Program, NIH (EB-011556, NS-078791, NS-082518), American Heart Association (14EIA8970041) and the Coulter Foundation. The authors also acknowledge the Texas Advanced Computing Center (TACC) at the University of Texas at Austin for providing HPC resources that have contributed to the research results reported within this paper. URL: <http://www.tacc.utexas.edu>.